Gain, detuning, and radiation patterns of nanoparticle optical antennas

C. Huang, A. Bouhelier,* G. Colas des Francs, A. Bruyant,† A. Guenot, E. Finot, J.-C. Weeber, and A. Dereux
Institut Carnot de Bourgogne, CNRS-UMR 5209, Université de Bourgogne, 21078 Dijon, France
(Received 4 August 2008; published 7 October 2008)

For their capability to localize and redirect electromagnetic field, metal nanoparticles have been recently viewed as efficient nanoantenna operating in the optical regime. In this article, we experimentally investigated the optical responses of coupled gold antenna pairs and measured the critical parameters defining antenna characteristics: resonant frequencies and bandwidths, detuning and gains, and radiation patterns.

DOI: 10.1103/PhysRevB.78.155407 PACS number(s): 42.30.Va, 73.22.Lp, 78.67.Bf

I. INTRODUCTION

Optical antennas are fundamental devices for interfacing light wave to nanoscale elements because of their capability to drastically confine and direct incoming radiation to relevant dimensions.[1–3] In the optical regime, this property originates from surface plasmon resonances and scattering properties of metal nanoparticle(s) constituting an optical antenna. Understanding the optical response of antenna/metal nanoparticles has therefore been a center of interest from the designer point of view. It is interesting to note that mainly two particle-dependent quantities are driving research efforts for fabricating optimal optical antennas. First, it was realized that radiowave antenna concepts are not fully applicable in the optical regime. To correctly design the dimensions of an optical antenna, an effective wavelength taking into account the surface plasmon resonant frequency was introduced.[4–7] Single-particle dark-field spectroscopy is usually employed to provide the spectral location of resonances, giving thus insights about dimensions of an antenna[8] and possible near-neighbor coupling mechanisms.[9,10] Second, optical antennas characterized by strong plasmon resonances provide an important mechanism for locally amplifying electromagnetic field. This characteristic is of particular interest to enhance weak optical responses such as single-molecule Raman scattering.[11] The field enhancement factor of a given antenna geometry is generally deduced from measurements involving the optical response to amplify: Raman scattering,[12] fluorescence,[7] or nonlinear photoluminescence.[1,13,14] While these type of signals inform about antenna's amplification at the molecular probe *emission* wavelength, they do not directly provide antenna's property at the wavelength used to *excite* them. Furthermore, the spectroscopic response of metal nanoparticles is known to be extremely sensitive to the surrounding environment. An external molecular reporter has therefore a perturbative influence on antenna characteristics.[15]

In this article, we report on nonperturbative experimental investigations of single optical antennas constituted of individual gold nanoparticles and dimers. In particular, we measured important parameters defining an optical antenna: spectral coverage, detuning, bandwidth, gain, and partial radiation pattern. To the difference with previous studies involving molecular probes, we are measuring antennas' characteristics at the excitation frequency, providing thus an important experimental tool to the designer.

II. EXPERIMENT

Our approach essentially relies on the experimental measurement of the partial local electromagnetic density of states (LDOS) obtained by integrating the differential scattering cross section of the antenna.[16] The LDOS uniquely describes the available optical eigenmodes in which photons can exist at a specific spatial location,[17] and any resonances occurring in an antenna will be encoded in the measured signal. Our apparatus, schematically described in Fig. 1(a), is based on efficient Fourier filtering of the specular scattered modes. As opposed to confocal dark-field microscopy,[18] our detection scheme retains only the frustrated evanescent components of the antenna (a more detailed description can be found in Ref. 16). The integrated forward-scattered intensity is detected in the image plane of the microscope by a photomultiplier (PMT) in a confocal-type arrangement. The antennas are scanned through the excitation and detection volumes to reconstruct an image of the scattering magnitude. The alignment of the illumination and detection was adjusted in the axial direction to maximize the scattered intensity detected and to reduce the point-spread function to a diffraction-limited response. To obtain the radiation diagram of the antennas, a charge-coupled device (CCD) appropriately placed at the Fourier plane (conoscopic detection) records the angular distribution of the evanescent modes collected by the 1.45 N. A. collection objective. More details on the arrangement will be given in Sec. IV.

The antennas were fabricated by electron-beam lithography followed by standard lift-off procedure and gold thermal evaporation. The nanoparticles forming the antennas have a varying diameter ranging from 66 to 90 nm and a height of ca. 70 nm. For the dimer antennas, the distance between particles (edge-to-edge) was systematically varied from 140 nm down to contact with a minimum separation distance of 10 ± 2 nm. Figure 1(b) shows electron micrographs of dimer antennas together with close up images of selected pairs. The spacing between dimers was kept constant to 3 μm to avoid any significant array-induced optical coupling between dimers.

III. DETUNING AND GAIN OF OPTICAL ANTENNAS

Figure 2 shows a two-dimensional scan of the scattered intensity from an array of individual antennas at an excitation wavelength $\lambda_{exc}=633$ nm. The polarization of the inci-

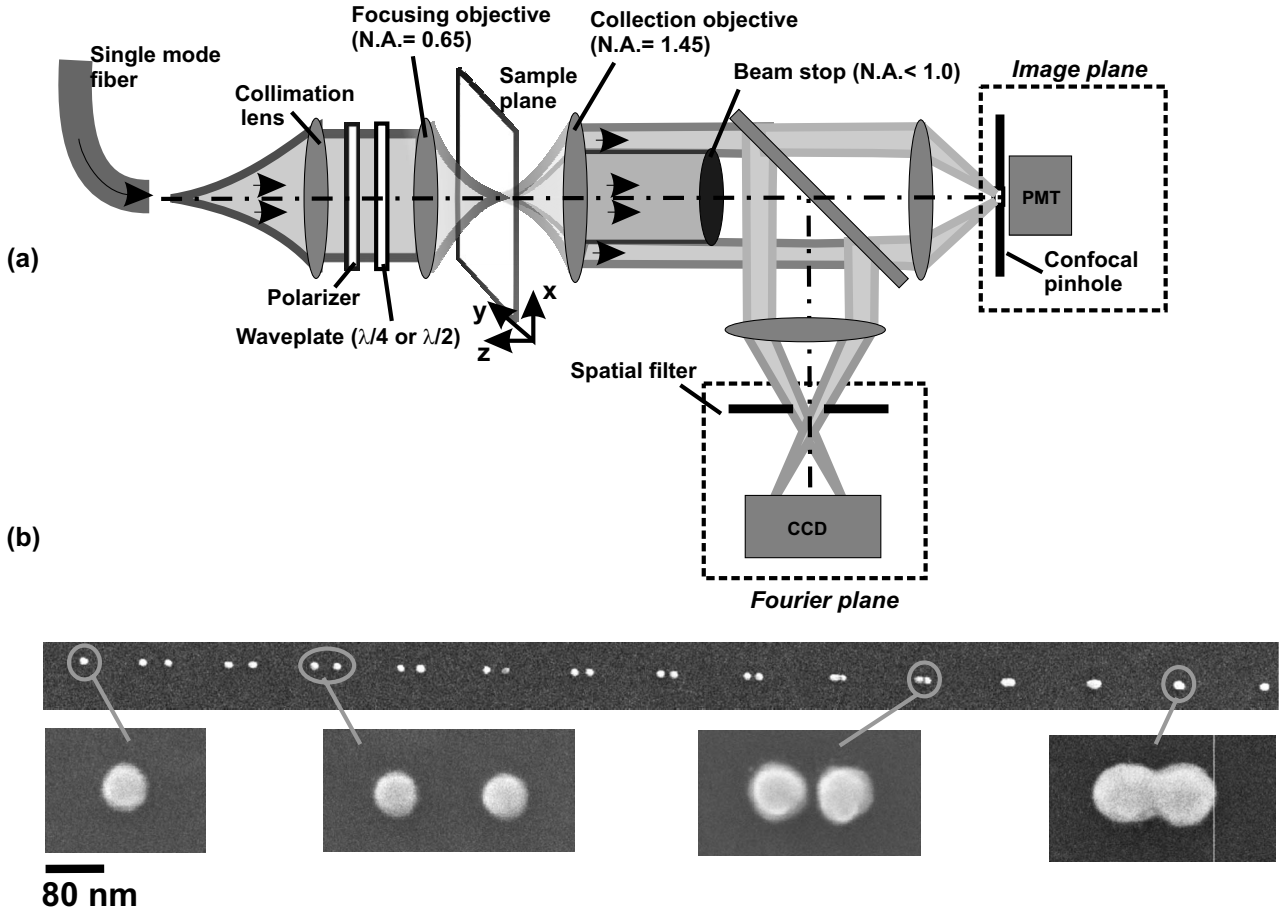

FIG. 1. (a) Experimental scheme. The antennas are illuminated by a 0.65 N. A. objective and the scattered components are collected by a 1.45-N. A. lens. The evanescent scattered angular spectrum is Fourier selected by a beam stop. (b) Electron micrographs of some of the antennas characterized in this study.

dent light was oriented along the dimer [Fig. 2(a)] or perpendicular to it [Fig. 2(b)] as indicated by the white arrows. The diameter of the antennas and the gap distance were systematically varied within the array [dotted arrows on the left and on the top of Fig. 2(a)] from 66 nm to 90 nm and from contact to approx. 140 nm, respectively. The first column on the left corresponds to scattering from single gold nanoparticles whereas the last two columns on the right of the array are bridged particles [see electron micrographs in Fig. 1(b)].

For a given polarization, the magnitude of the scattered intensity is not constant within the array. In Fig. 2(a) for instance, the brightest antennas appear for larger particle diameters and smaller gaps consistent with an increase in the scattering cross section for larger particles. Figures 2(c) and 2(d) are three-dimensional (3D) renderings of the boxed lines in Figs. 2(a) and 2(b). For a polarization oriented along the dimer, the scattered intensity increases by reducing the gap between dimers before an abrupt falloff for the last two antennas (bridged particles: red circle). Interestingly, Fig. 2(d) shows an almost constant intensity regardless of the gap even for the two particles that are in contact (red circle).

To gain understanding on these intensity variations, we systematically measured scattered spectra from individual coupled antennas using dark-field spectroscopy. Typical spectra scattered from a single dimer with an approximate 10-nm gap and 70-nm diameter are shown in Fig. 3(a) for unpolarized illumination and for a polarization parallel and perpendicular to the dimer axis, respectively. As the result of a strong coupling between the two interacting particles, a well-known hybridization of the resonance occurs.[19,20] Figure 3(b) shows typical dependence of the resonance maxima λ_{sp} for varying gaps and for particle diameter of 80 nm. The vertical bars indicate the full width at half maximum of the resonances. The splitting of λ_{sp} starts for particle separation below 30 nm and a redshift of λ_{sp} is observed for a polarization oriented along the main axis of the antennas in accordance with the literature.[21,22] We note that averaged measurements on large arrays of coupled nanoparticles revealed a small blueshift of the resonance for an electric field perpendicular to the main axis.[21] We do not see such a shift in our single-dimer measurements. Instead, we measured a systematic redshift of the resonances [Fig. 3(b)]. We attribute this difference to the unique fingerprints of individual dimers. These individual different responses can also be observed from dimers with large gaps (>50 nm) whereby the position of the maxima exhibits spectral oscillations despite nominally comparable particles [Fig. 3(b)].

To correlate the variations in the scattered intensity at the laser frequency with the spectral signature of the antenna, we define the amount of detuning $|\delta\lambda|$ by differentiating the la-

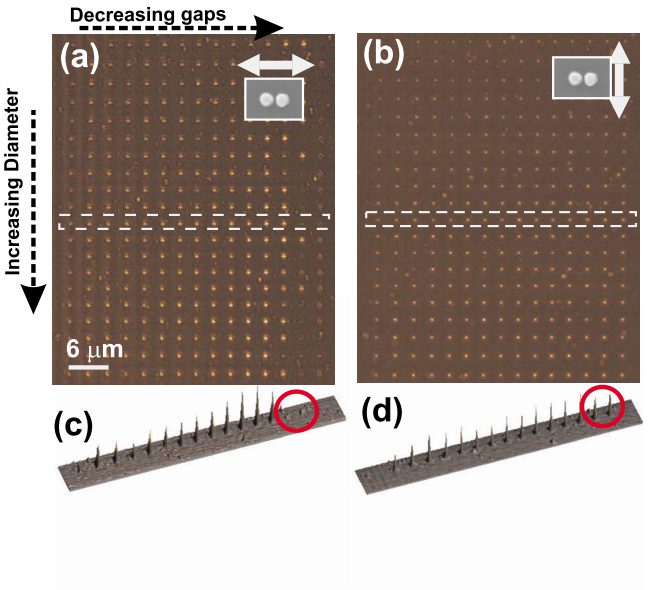

FIG. 2. (Color online). (a) and (b): Scattering intensities at $\lambda = 633$ nm from single antennas constituted of gold nanoparticle dimers for a polarization parallel to the dimer axis and perpendicular to it, respectively (white arrows). The first column on the left is single-particle antenna, and the two last columns on the right are bridged particles. Top line displays particles with diameter of 60 nm increasing up to 90 nm for the bottom line. (c) and (d) are 3D rendering of the dotted line in (a) and (b).

ser wavelength to the resonance maxima: $|\delta\lambda| = |\lambda_{exc} - \lambda_{sp}|$. Let us also introduced the relative gain G of an antenna. In antenna theory, G describes the ability of an antenna to increase scattered intensity in the direction of the peak radiation. This parameter is usually normalized from a reference radiator, i.e., a dipole.[23] For small particles compared to the wavelength of light, an isolated spherical nanoparticle behaves essentially like a dipole. We therefore define G by measuring the magnitude of the scattered intensities I_d originating from dimers and normalizing it to the one issued from single-particle antennas I_s of the same diameter: $G = I_d / I_s$. This definition assumes that the scattered angular distribution and the collection efficiency of our experimental setup are constant regardless of the particle arrangement. The validity of this assumption will be asserted in Sec. IV.

Figure 4(a) shows the evolution of the parameters $|\delta\lambda|$ and G by reducing the gap between the dimer and for an excitation field at 633 nm polarized along the dimer axis. For large gaps (>50 nm), detuning from the excitation laser $|\delta\lambda|_{633\ nm}$ is kept below 25 nm, indicating that the antennas are close to resonance with the laser line. This is confirmed by the trend of the G factor, which varies around 2.5. For a group of identical particles characterized by a weak mutual optical interaction, G should scale linearly with the number of particle present in the detection volume if the excitation is homogeneous. However, the measured value is slightly larger than the expected value ($G=2$). We think this small difference originates from the polarization-sensitive inhomogeneous field distribution inside the excitation and detection volumes.[24,25]

For smaller gaps, a strong electromagnetic coupling between the particles constituting the antenna rapidly increases

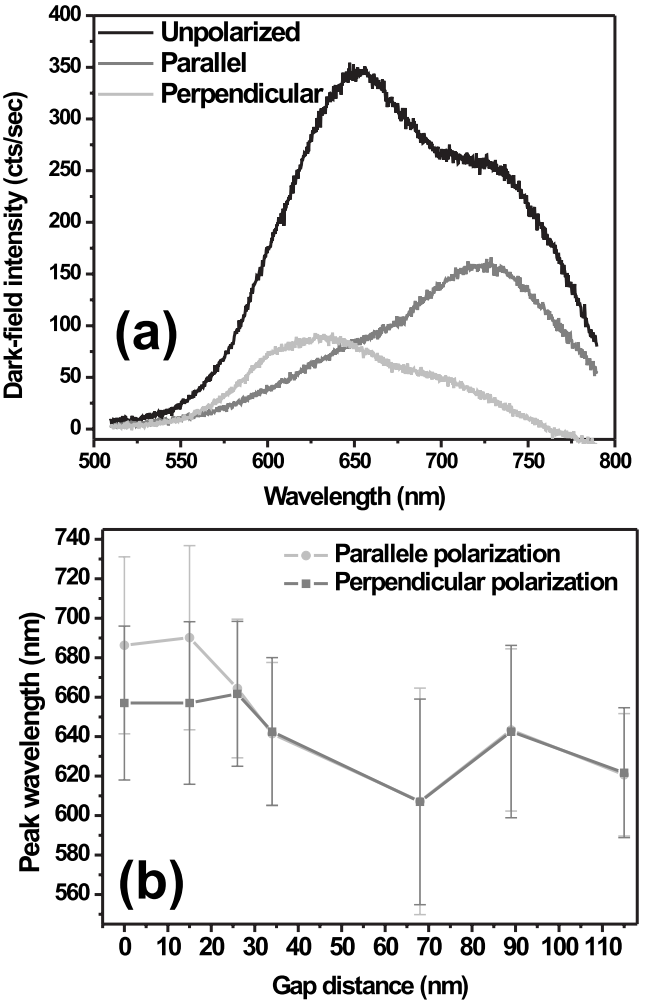

FIG. 3. (a) Characteristic spectra for an isolated strongly coupled dimer. The unpolarized spectrum (black) features two polarization-sensitive resonances identified by a polarized excitation (dark gray and gray). Gap ~ 10 nm and particle diameter 70 nm. (b) Dependence of the dimer resonance(s) on the gap values. For small gaps, a redshift and a hybridization of the resonances are observed. The vertical bars indicate the breadth of the resonances. The particle diameter is 80 nm.

the amount of detuning and $|\delta\lambda|_{633\ nm}$ reaches 55 nm for a 15-nm gap. In this coupling regime, G dramatically drops from a maximum of 3.3 to a value of 0.3 for the bridged dimer, indicating that the optical antenna is detuned from its optimum excitation frequency.

Figure 4(b) shows the trend of $|\delta\lambda|_{633\ nm}$ and G for a polarization oriented perpendicular to the dimer. $|\delta\lambda|_{633\ nm}$ oscillates around 15 nm and stays within the full width at half maximum of the surface plasmon resonances [see Fig. 3(b)]. The gain features two plateaux of almost constant G values ($G=2.3$ and 1.6 with variations ~10%) for gaps below 50 nm and gaps above 50 nm, respectively. Since $|\delta\lambda|_{633\ nm}$ stays near resonance with the excitation line and G is close to its expected value of 2, we also attribute these two plateaux to the particularity of the focal field distribution: it's only when the particles are close to each other that the excitation intensity can be assumed to be spatially constant. We

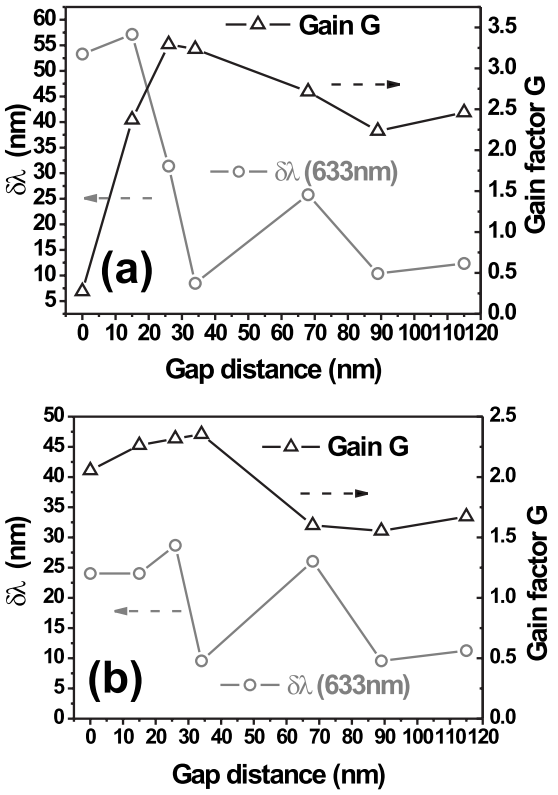

FIG. 4. (a) and (b): Detuning factor $|\delta\lambda|_{633\ \mathrm{nm}}$ (gray) and gain factor G (black) for parallel and perpendicular polarizations with respect to the dimer axis, respectively. Particle diameter: 80 nm.

note that the experimental magnitude of G does not reach very large enhancement values as predicted from strongly coupled nanoparticle pairs and small gaps.[26,27] This relatively low gain have also been observed in Ref. 28. It is worth emphasizing that the enhancement factors calculated in the literature are usually normalized to the applied field, whereas in the present work we compare G to a reference dipolar antenna. We note that $|\delta\lambda|_{633\ \mathrm{nm}}$ and to some extend G show some oscillatory behavior with increasing gap distance. This particularity is observed regardless of the particle size within the fabricated array and polarization orientation. We did not see in our measurement a systematic correlation between the positions of the oscillatory peaks and the interparticle distance. We therefore believe that the observed oscillations are resulting from variations in the antenna morphology inherent to the fabrication process.

In only one instance in the study of the array depicted in Fig. 2(a) was G significantly increased. Figure 5 shows experimental values of G and $|\delta\lambda|_{633\ \mathrm{nm}}$ for the upper most line of the array (particle diameter is 66 nm) and a polarization oriented along the axis joining the dimers. In this graph, we observed typical spectral variation in $|\delta\lambda|_{633\ \mathrm{nm}}$ for large gaps already seen in Fig. 4(a). The gain factor is constant for the two largest gaps ($G\sim 2$) and displays a small increase for the 37-nm-gap dimer consistent with the low value of $|\delta\lambda|_{633\ \mathrm{nm}}$. For smaller gaps however, the antennas are being detuned and yet G keeps increasing to reach a value of 6.3 for the 18-nm-gap dimer. G undergoes then an abrupt falloff for the bridged pair. Despite the antennas being detuned with

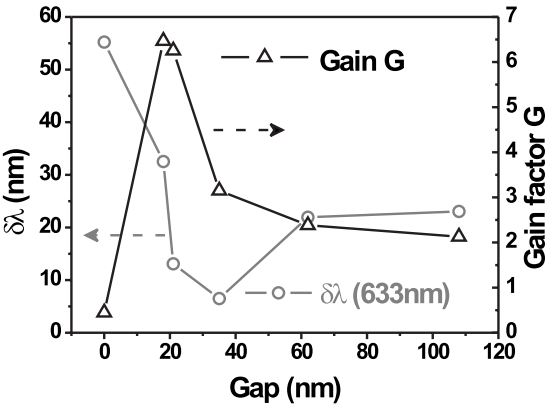

FIG. 5. Detuning factor $|\delta\lambda|_{633\ \mathrm{nm}}$ and gain factor G for parallel with respect to the dimer axis, respectively. Particle diameter is 66 nm.

respect to the laser line, the optical coupling and field amplification characterizing these particular antennas were sufficient to not only compensate G for the detuning of the antenna but also enhance it by a sixfold factor. The measured gain for this coupled antenna was not reproduced inside the fabricated array and emphasizes the difficulty to design electromagnetic hotspots by such fabrication technique.

To validate our approach, we investigated the antenna array depicted in Fig. 2 at a laser wavelength of 780 nm. Figure 4(a) demonstrated a rapid decrease in G when the antennas are red detuned from the excitation at 633 nm. It is therefore expected that by reducing the detuning by using a 780-nm laser line, the gain will be restored. Figure 6(a) displays the evolution of G and $|\delta\lambda|_{780\ \mathrm{nm}}$ for the same set of antennas featured in Fig. 4(a) and for a polarization parallel to the dimer. For decreasing gaps, $|\delta\lambda|_{780\ \mathrm{nm}}$ also decreases as a consequence of the redshift of the resonance, and as hypothesized, strongly coupled dimers exhibit a significant recovering of G. To the difference with an illumination at 633 nm, antennas characterized by small gaps are tuned toward resonance for a 780-nm-excitation line. It should be noted that the relatively high values of G (up to $G\sim 17$) originate from the weak intensity I_s scattered by the referenced single particle. This single-particle antenna is not at resonance at 780 nm.

Figure 6(b) showed the case for a perpendicular polarization. $|\delta\lambda|_{780\ \mathrm{nm}}$ indicates that the antenna is significantly detuned for this polarization regardless of the gap size. Accordingly, the antenna gains have low values compared to the orthogonal polarization. Nonetheless, a slow decrease in $|\delta\lambda|_{780\ \mathrm{nm}}$ for small gaps is observed concomitant to a twofold increase in G.

IV. RADIATION PATTERNS OF OPTICAL ANTENNAS

With radio-frequency antenna,[23] the radiated power at large distances is the parameter of interest, and radiation patterns are traditionally measured considering the antenna in an homogenous dielectric medium. Optical antennas, however, are typically fabricated on a substrate and the presence of an interface considerably modifies the radiation pattern.

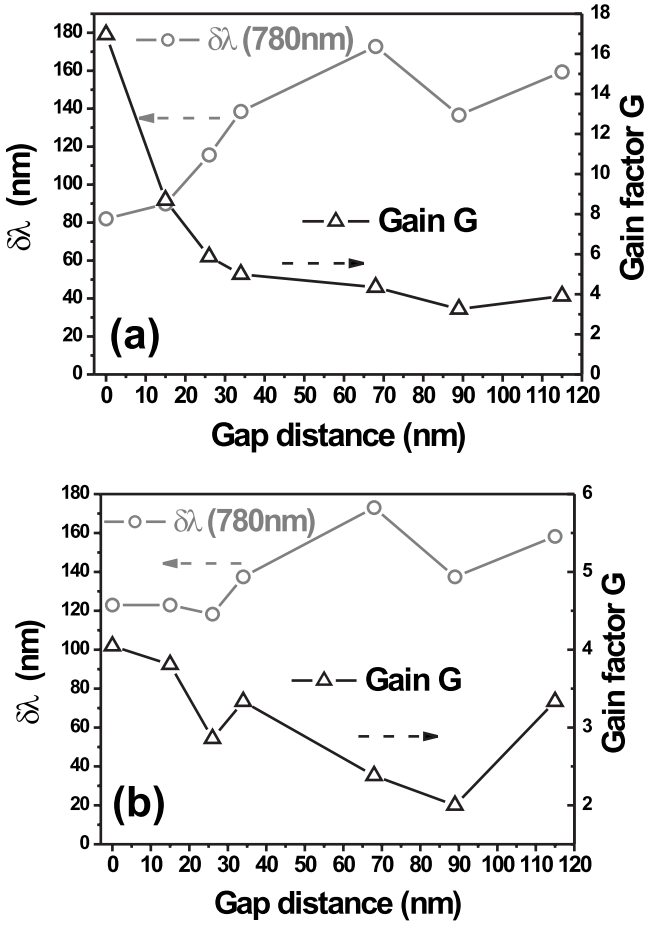

FIG. 6. (a) and (b) Detuning factor $|\delta\lambda|_{780\ \mathrm{nm}}$ and gain factor G for a 780-nm excitation wavelength and for a polarization oriented along the dimer axis and perpendicular to it, respectively. Particle diameter is 80 nm.

For small particles behaving like dipoles close to a dielectric interface, the radiated power is principally emitted in the denser medium at the critical angle,[29] and backward scattering can be neglected. We use a 1.45 oil-immersion objective [Fig. 1(a)] to retrieve this forward-scattered contributions. At the exit pupil of the objective, i.e., the primary Fourier plane, the angular distribution of the scattered intensity is a direct measure of the radiation pattern in the substrate. With modern objective lenses, however, this primary Fourier plane is located inside the objective's body, and relay lenses are usually employed to image the objective's back aperture at a secondary Fourier plane.[30–34]

To retrieve the near-field contribution and to discriminate it from the overwhelming illumination contribution, a beam stop removes the part of the light angularly distributed below the critical angle as sketched in Fig. 1(a). The filtering only retains radiated intensity corresponding to frustrated evanescent modes of the antenna collected by our objective, i.e., its partial induction field. In the following, the term radiation patterns will be referred to the angular distribution of the scattered intensity located above the critical angle and is therefore a partial measure of the total pattern.

Figure 7 shows experimental scattered diagrams for an optical antenna constituted of a single colloidal 80-nm Au

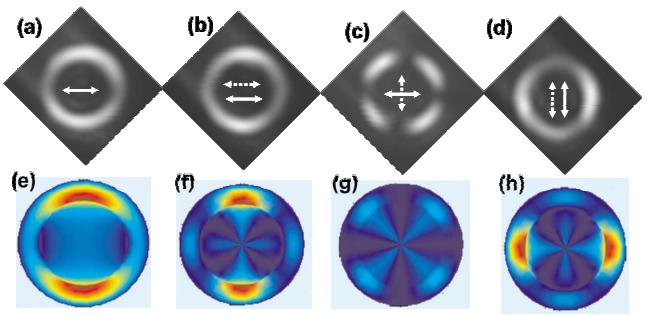

FIG. 7. (Color online). (a) to (d) Angular distributions of the intensity scattered by a single Au nanoparticle. The white arrow indicates the incident polarization and the broken arrow the analyzer orientation. The intensity peaks at the critical angle. (e) to (h) are the corresponding calculated intensity distributions.

nanoparticle illuminated by $\lambda_{exc}=633$ nm. Here we choose to utilize perfectly spherical nanoparticles from a colloidal solution to set a reference for the following and to avoid any shape-induced artifacts remnant with electron-beam lithography. Figure 7(a) represents the intensity distribution for a polarization indicated by the thick arrow. Two lobes perpendicularly oriented to the polarization are observed peaking at the critical angle. These lobes are characteristic from a dipole emission oriented parallel to a dielectric interface.[31] This scattered pattern is in very good agreement with our numerical calculation of a dipole emission shown in Fig. 7(e). Figures 7(b) and 7(c) display the scattered diagram of the same particle analyzed through parallel and cross polarizers, respectively (broken arrow). Note that all the experimental images are rotated to compensate for a 45° tilt of the outport of our microscope. Figures 7(f)–7(h) are numerical simulations of the dipole emissions corresponding to the experimental polarizer and analyzer orientations. Note that all angles below θ_c were included in the calculations. A significant portion of the intensity is located in the vicinity of θ_c, indicating that our Fourier filtering rejects a negligible portion of the scattered diagram.

We now turn our attention to the scattered pattern of the antennas constituted of coupled pairs of nanoparticles. Arrangement of strongly interacting core-shell nanoantennas were predicted to significantly modify radiation patterns.[35] For coupled dimers, however, the angular emission is almost unaffected and only the intensity distribution is modified. Figures 8(a)–8(c) shows diagrams for selected antennas with gap values of 126, 68, and 15 nm, respectively. The diameter of individual nanoparticles was fixed at 80 nm. The polarization is aligned with the dimer axis and the illumination wavelength is 633 nm. Figure 8(d) shows the 15-nm-gap antenna pattern for a polarization oriented perpendicularly to the dimer axis. These scattered diagrams do not significantly differ from the diagrams characterizing the single-particle antenna showed in Fig. 7: the intensity distribution is peaked at the critical angle and the two-lobe patterns are readily recognized. These antennas essentially have a dipolar response of their radiation pattern. However, a close inspection reveals some differences. Let us define the contrast ratio η:

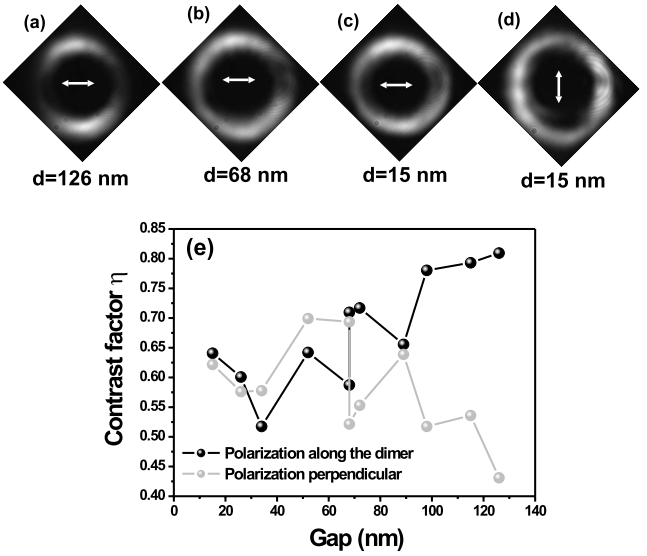

FIG. 8. (a) to (c) Angular distributions of the intensity scattered by dimers with varying gaps d and with an excitation field oriented along the dimer. (d) Polarization oriented perpendicular to a 15-nm-gap dimer. (e) Evolution of the contrast η for the two polarizations.

$$\eta = \frac{I_{\max} - I_{\min}}{I_{\max} + I_{\min}}, \tag{1}$$

where $I_{\max}$ and $I_{\min}$ are the orthogonal intensity maxima and minima of the scattered diagram. The η parameter indicates the deviation of the antennas' scattered diagram from an ideal dipole pattern. For reference, the values of contrast ratio extracted from the colloidal particle emission pattern of Fig. 7(a) and calculated dipolar diagram of Fig. 7(e) are in agreement at $\eta=0.5$. Here, however the reference isolated single particle yields a higher value of $\eta=0.72$ for the two polarizations and does not significantly change with the diameter of the particles investigated. The difference of contrast between the scattered diagram of a colloidal nanoparticle and lithographed particle of nominally similar diameters remains unclear, but is probably linked to the different morphology of the later particle type. Figure 8(e) shows the evolution of the contrast ratio η for varying gaps and for the two orthogonal orientations of the incident field. Interestingly, θ_c has an opposite trend between the two polarizations. For an incident field oriented along the axis of the dimer and for wider gaps, η increases and reaches a value comparable to the reference isolated particle ($\eta=0.72$). This is clearly indicating a reduced interaction between the two particles for large gaps. On the contrary, for a polarization perpendicular to the dimer, η is approaching the reference contrast of an isolated particle for the shortest dimer separation. The magnitude of $I_{\max}$ does not significantly vary across the different antennas (variation $<5\%$). The evolution of η is mainly governed by the value of $I_{\min}$. We attribute the trends of η to a modification of the azimuthal radiation direction for antennas characterized by interacting nanoparticles: for a polarization along the dimer, the particles are more likely to interact in the near field since the far-field radiation pattern of individual particles are oriented perpendicular to the electric field. For the orthogonal polarization, however, the far-field radiation patterns of the two particles are aligned with the main axis of the dimer, and the interaction is therefore stronger for larger gaps.

V. CONCLUSIONS

For their ability to interface free-space radiation with nanoscale elements and devices, optical antennas are likely to play a major role in the next generation of photonic devices and sensors. Knowing the important parameters defining the properties of individual optical antennas is therefore essential for this goal. We have developed experimental techniques to rapidly compare the basic units constituting an optical antenna and measure their critical performances. By only retaining a part of the evanescent spectrum scattered by individual nanoantennas and by correlating the magnitude of this signal with their spectral characteristics, we experimentally measured the gain and the detuning factors for a given excitation wavelength. We also recorded radiation patterns of various type of antennas and found that their partial radiation pattern is essentially dipolar in nature. Important is the fact that our approach allows us to characterize the antennas at the excitation frequency. It does not require the use of reporter molecules or nonlinear phenomena to probe the antenna's response and is therefore completely nonperturbative.

ACKNOWLEDGMENTS

A.B. is grateful to R. Zia (Brown University) for his helpful comments about Fourier planes. The authors thank the Agence Nationale de la Recherche (ANR) under Grants Antares (PNANO 07-51) and Photohybrid (BLANC 07-2-188654), as well as the Regional Council of Burgundy (program FABER) for funding. C. H. acknowledges stipend from the People's Republic of China.

*Corresponding author: alexandre.bouhelier@u-bourgogne.fr

†Present address: Laboratoire de Nanotechnologie et d'Instrumentation Optique ICD CNRS-FRE 2848, Université de Technologie de Troyes, 10000 Troyes, France.

[1] P. Mühlschlegel, H.-J. Eisler, O. J. F. Martin, B. Hecht, and D. W. Pohl, Science **308**, 1607 (2005).

[2] E. Cubukcu, E. A. Kort, K. B. Crozier, and F. Capasso, Appl. Phys. Lett. **89**, 093120 (2006).

[3] T. Taminiau, F. D. Stefani, and N. F. Van Hulst, Opt. Express **16**, 16858 (2008).

[4] J. Aizpurua, G. W. Bryant, L. J. Richter, F. J. García de Abajo, B. K. Kelley, and T. Mallouk, Phys. Rev. B **71**, 235420 (2005).

[5] P. J. Burke, S. Li, and Z. Yu, IEEE Trans. Nanotechnol. **5**, 314 (2006).

[6] L. Novotny, Phys. Rev. Lett. **98**, 266802 (2007).
[7] T. H. Taminiau, R. J. Moerland, F. B. Segerink, L. Kuipers, and N. F. van Hulst, Nano Lett. **7**, 28 (2007).
[8] J. Mock, M. Barbic, D. R. Smith, D. A. Schultz, and S. Schultz, J. Chem. Phys. **116**, 6755 (2002).
[9] D. P. Fromm, A. Sundaramurthy, P. J. Schuck, G. Kino, and W. E. Moerner, Nano Lett. **4**, 957 (2004).
[10] A. Bouhelier, R. Bachelot, J. Im, G. P. Wiederrecht, G. Lerondel, S. Kostcheev, and P. Royer, J. Phys. Chem. B **109**, 3195 (2005).
[11] K. Kneipp, H. Kneipp, and J. Kneipp, Acc. Chem. Res. **39**, 443 (2006).
[12] S. Lal, N. K. Grady, G. P. Goodrich, and N. J. Halas, Nano Lett. **6**, 2338 (2006).
[13] P. J. Schuck, D. P. Fromm, A. Sundaramurthy, G. S. Kino, and W. E. Moerner, Phys. Rev. Lett. **94**, 017402 (2005).
[14] A. Bouhelier, R. Bachelot, G. Lerondel, S. Kostcheev, P. Royer, and G. P. Wiederrecht, Phys. Rev. Lett. **95**, 267405 (2005).
[15] J. N. Anker, W. P. Hall, O. Lyandres, N. C. Shah, J. Zhao, and R. P. V. Duyne, Nature Mater. **7**, 442 (2008).
[16] C. Huang, A. Bouhelier, G. Colas des Francs, G. Legay, J.-C. Weeber, and A. Dereux, Opt. Lett. **33**, 300 (2008).
[17] G. Colas des Francs, C. Girard, J. C. Weeber, C. Chicane, T. David, A. Dereux, and D. Peyrade, Phys. Rev. Lett. **86**, 4950 (2001).
[18] O. L. Muskens, V. Giannini, J. A. Sánchez-Gil, and J. Gómez Rivas, Opt. Express **15**, 17736 (2007).
[19] H. Tamaru, H. Kuwata, H. T. Miyazaki, and K. Miyano, Appl. Phys. Lett. **80**, 1826 (2002).
[20] P. Nordlander, C. Oubre, E. Prodan, K. Li, and M. I. Stockman, Nano Lett. **4**, 899 (2004).
[21] W. Rechberger, A. Hohenau, A. Leitner, J. Krenn, B. Lamprecht, and F. Aussenegg, Opt. Commun. **220**, 137 (2003).
[22] I. Romero, J. Aizpurua, G. W. Bryant, and F. J. García de Abajo, Opt. Express **14**, 9988 (2006).
[23] T. A. Milligan, *Modern Antenna Design* (Wiley, New York, 2005).
[24] L. Novotny, D. R. Grober, and K. Karrai, Opt. Lett. **26**, 789 (2001).
[25] M. R. Beversluis, A. Bouhelier, and L. Novotny, Phys. Rev. B **68**, 115433 (2003).
[26] H. Xu and M. Käll, Phys. Rev. Lett. **89**, 246802 (2002).
[27] E. Hao and G. C. Schatz, J. Chem. Phys. **120**, 357 (2004).
[28] A. L. Lereu, G. Sanchez-Moistero, P. Ghenuche, R. Quidant, and N. F. V. Hulst, J. Microsc. **229**, 254 (2008).
[29] W. Lukosz and R. E. Kunz, J. Opt. Soc. Am. **67**, 1607 (1977).
[30] A. Bouhelier, M. Beversluis, A. Hartschuh, and L. Novotny, Phys. Rev. Lett. **90**, 013903 (2003).
[31] A. Lieb, J. M. Zavislan, and L. Novotny, J. Opt. Soc. Am. B **21**, 1210 (2004).
[32] A. Drezet, A. Hohenau, A. L. Stepanov, H. Ditlbacher, B. Steinberger, N. Galler, F. R. Aussenegg, A. Leitner, and J. R. Krenn, Appl. Phys. Lett. **89**, 091117 (2006).
[33] M. U. Gonzàlez, A. L. Stepanov, J. C. Weeber, A. Hohenau, A. Dereux, R. Quidant, and J. R. Krenn, Opt. Lett. **32**, 2704 (2007).
[34] S. Massenot, J. Grandidier, A. Bouhelier, G. Colas des Francs, L. Markey, J.-C. Weeber, A. Dereux, J. Renger, M. U. Gonzàlez, and R. Quidant, Appl. Phys. Lett. **91**, 243102 (2007).
[35] J. Li, A. Salandrino, and N. Engheta, Phys. Rev. B **76**, 245403 (2007).